A COUPLED PRESCRIBED WAKE-EULER SOLVER FOR EFFICIENT COMPUTING HELICOPTER ROTOR FLOWS IN HOVER

Kazem Hejranfar and Masoud Mohammadi
Aerospace Engineering Department, Sharif University of Technology, Tehran, Iran

Keywords: *Rotor Flow, Perturbation Method, Prescribed Wake Model, Unstructured Grids*

Abstract

A numerical solution technique is developed to simulate the flowfield of hovering helicopter rotor. The present method uses a coupled prescribed wake-Euler solver to efficiently allow the vortical wake effects. The three-dimensional Euler equations written in a rotating coordinate frame are solved by using a cell-centered finite volume scheme that is based on the Roe's flux-difference splitting on unstructured meshes. High-order accuracy is achieved via the reconstruction of flow variables using the MUSCL interpolation technique. Calculations are carried out for an isolated rotor in hover for two operating conditions of subsonic and transonic tip Mach numbers, $M_{tip} = 0.44$ *and* $M_{tip} = 0.877$*, and the collective pitch angle* $\theta_c = 8°$ *(the Caradona and Tung test cases). The computed surface pressure distributions for each case are compared with available numerical and experimental data. The results indicate that for conventional grids, the calculated surface pressure distributions do not agree with the experimental data especially at inboard sections of the blades. This difference may be due to the fact that the numerical methods using course grids have inherent numerical dissipation which can affect the structure of the rotor wake. To improve the computed results, a perturbation method is used and wake effects are modeled using only a tip vortex trailed from the tip of each blade. The resulting surface pressure distributions using the proposed technique exhibit good agreement with the numerical and experimental results, especially for the subsonic case.*

1 Introduction

The accurate numerical simulation of the helicopter rotor flow in hover or forward flight leads to an accurate calculation of rotor blade aerodynamic loads. The flowfield around a rotor is difficult to model due to the presence of vortical wake and transonic flow near the tip of blades. The complexity of the rotor flowfield results from effects of strong vortical wake and primary vortical structures that are convected away from the rotor disk at relatively low speeds. The vortical wake of rotor, consists of the inboard vorticity region (the vortex sheet) and the tip vortex, induces a three-dimensional induced flowfield that reduces the effective pitch angle of each blade and consequently affects the aerodynamic characteristics of rotor blades. Thus, flow solvers have to be able to accurately resolve the vortical wake of rotor.

Potential flow solvers simplify the mathematical formulation and achieve efficient solutions for rotor flows [1,2]. Although the potential flow methods can and should be used whenever possible, it is desirable to use computational methods that can complement these solvers when the potential flow assumption breaks down. One of the drawbacks of using potential solvers is that potential flow formulation does not admit for distributed vorticity in the flowfield. For rotor flows, a large portion of the flowfield near the blades is rotational. In addition, potential flow solvers can not accurately predict the aerodynamic characteristics near the tip region of the blades where compressibility effects are significant and the flow may be in transonic regime.

Euler/Navier-Stokes schemes can accurately compute subsonic/transonic flowfields around a rotor and admit the vortical solutions. However, Euler/Navier-Stokes solvers using conventional numerical methods and grids are unable to capture the vortical flowfields due to high levels of numerical viscosity present in these schemes, particularly on course grids far away from the rotor disk. A number of Euler/Navier-stokes solvers have been developed to simulate helicopter rotor flowfields. Some of these solvers have used high-order accuracy methods with fine grids [3-7] or used grid refinement/adaptation schemes [8.9] to accurately solve the vortical flowfields and capture the shed vorticity and the tip vortices. However, these methods require significant computer resources. Some attempts have been focused to reduce the computational time through the use of a hybrid Navier-Stokes/full potential method [10-12]. Another way is to use artificial far field boundary conditions, e.g. a sink placed at rotor hub to create the correct inflow [13].

One alternative to accurately compute the helicopter rotor flow is to use a coupled free wake-CFD solver. A number of coupled free wake-CFD methods have been used to simulate the vortical wake for rotor flow and include realistic wake effects [14,15]. In these solvers, both the inboard vortex sheet and the tip vortices are modeled. For rotor flow due to high loading near the tip of the blades, the use of tip vortices, instead of full wake modeling, may determine the correct induced flowfield and consequently the rotor aerodynamic loads in an efficient manner.

The objective of the present work is to develop an efficient and more economical flow solver for accurate computation of the aerodynamic characteristics of helicopter rotor in hover. The method presented herein uses a coupled prescribed wake-Euler solver to efficiently allow the vortical wake effects. The computational domain consists of unstructured tetrahedral cells. The numerical method used is a cell-centered finite volume scheme that is based on the Roe's flux-difference splitting [16] on unstructured meshes. For a high-order scheme, the estimation of the flow variables at each cell face is achieved by MUSCL formulation [17]. To efficiently model the vortical wake and improve the computed results, the Euler equations are coupled to a prescribed wake model that is incorporated into the finite-volume solver using a prescribed flow, or perturbation technique [14,18]. In the present study, the wake effects of each blade are modeled using only a tip vortex trailed at the tip of each blade and the effects of inboard vortex sheet is modeled implicitly by reducing the strength of the tip vortex. The initial geometry of tip vortex is constructed using the prescribed wake model introduced by Landgreb [19,20].

The present calculations are performed for an isolated rotor in hover and for two operating conditions of subsonic and transonic tip Mach numbers, $M_{tip} = 0.44$ and $M_{tip} = 0.877$, and for the collective pitch angle $\theta_c = 8°$. This test case was experimentally studied by Caradona and Tung [21]. The computed surface pressure distributions for each case with and without wake modeling are compared with numerical results as well as experimental data.

2 Governing Equations

Euler equations are a suitable set of equations for computing the subsonic/transonic flowfields around a rotor and admit the vortical solutions. The Euler equations are formulated in a rotating coordinate frame (x, y, z) attached to the rotor blades in terms of absolute-flow velocities. Therefore, the absolute flow in the far field remains uniform but the relative flow is nonuniform. For this coordinate system, x is in the chordwise direction, y is in the radial direction, and z is in the normal direction (Fig. 1). The inertial coordinates (x', y', z') are taken to coincide with (x, y, z) at an instant in time t. The computational domain consists of unstructured tetrahedral cells. The governing equations may be written in an integral form for an arbitrary grid cell as

$$\frac{\partial}{\partial t}\iiint_V \boldsymbol{Q}\, dV + \iint_{\partial V} \boldsymbol{F}(\boldsymbol{Q}).\hat{n}\, dS = \iiint_V \boldsymbol{S}(\boldsymbol{Q})\, dV \qquad (1)$$

where the solution vector of conservative variables $\boldsymbol{Q}$, the inviscid flux vector $\boldsymbol{F}(\boldsymbol{Q})$ and the source term $\boldsymbol{S}(\boldsymbol{Q})$, due to the centrifugal force of rotation of the blades, are given by

$$\boldsymbol{Q}=\begin{Bmatrix}\rho\\ \rho u\\ \rho v\\ \rho w\\ E\end{Bmatrix},\boldsymbol{F}(\boldsymbol{Q}).\hat{\boldsymbol{n}}=\begin{Bmatrix}\rho U_{\perp r}\\ \rho u U_{\perp r}+p\hat{n}_x\\ \rho v U_{\perp r}+p\hat{n}_y\\ \rho w U_{\perp r}+p\hat{n}_z\\ E U_{\perp r}+pV_n\end{Bmatrix},\boldsymbol{S}(\boldsymbol{Q})=\begin{Bmatrix}0\\ \rho\,\Omega\,v\\ -\rho\,\Omega\,u\\ 0\\ 0\end{Bmatrix}$$

where

$$E=\frac{p}{\gamma-1}+\frac{1}{2}\rho\,(u^2+v^2+w^2)$$

and V is the cell volume, $\hat{n}\,dS$ is a vector element of surface area with outward unit normal vector $\hat{\boldsymbol{n}}(\hat{n}_x,\hat{n}_y,\hat{n}_z)$, ρ is the density, p is the pressure, E is the total energy per unit volume, Ω is the angular velocity in the z direction relative to the inertial frame (x',y',z'), $\boldsymbol{V}=(u,v,w)$ is the absolute velocity vector in the Cartesian coordinates (x,y,z) where (u,v,w) are the absolute velocity components relative to the inertial frame (x',y',z'). In addition, $V_n=\boldsymbol{V}.\hat{\boldsymbol{n}}$ is the normal velocity component of flow, and $U_{\perp r}=(\boldsymbol{V}-\tilde{\boldsymbol{V}}).\hat{\boldsymbol{n}}=V_n-\tilde{V}_n$ is the normal relative velocity where $\tilde{\boldsymbol{V}}=(-\Omega y,\Omega x)$ is the grid velocity vector. The term $\tilde{V}_n$ is only a function of space and is fixed at each cell for the grid with constant rigid-body rotation. Also, the surface unit vector $\hat{\boldsymbol{n}}(\hat{n}_x,\hat{n}_y,\hat{n}_z)$ can be calculated only once without the rotational matrix being involved.

The preceding equations are nondimensionalized by the reference parameters. The density and pressure are normalized by their freestream values, ρ_∞ and p_∞, the total energy per unit volume by p_∞, the velocities by $a_\infty/\sqrt{\gamma}$ where a_∞ is the freestream speed of sound, and lengths by the rotor blade cord c and the time by $c\sqrt{\gamma}/a_\infty$. The ratio of specific heats for air is prescribed as $\gamma=1.4$.

Using the above nondimensionalization, the following definition for the angular velocity can be obtained

$$\Omega=\frac{\sqrt{\gamma}\,M_{tip}}{R}$$

where M_{tip} is the tip Mach number and $R=R^*/c$ is the nondimensional rotor radius or the rotor blade aspect ratio.

The above formulation in the rotating coordinate frame has in exactly the same form of the equations in the inertial frame, except for an additional source term which has been introduced into the right side of the equation and represents the centrifugal force of rotation of the blades. The preceding formulation using the absolute-flow velocities allows more accurate calculation of the fluxes in the finite-volume method on unstructured grids in the far field where the grid is highly stretched. In addition, the far field boundary conditions can be easily implemented.

3 Numerical Method

A finite-volume discretization is applied to Eq. (1) which describes a relationship where the time rate of change of the state vector $\boldsymbol{Q}$ within the domain V is balanced by the net fluxes of $\boldsymbol{F}$ and $\boldsymbol{F}(\boldsymbol{Q})$ across the boundary surface ∂V. The domain is divided into a finite number of unstructured tetrahedral cells and Eq. (1) is applied to each cell. The state variables $\boldsymbol{Q}$ are volume-averaged quantities.

In the present work for simulating rotor flows, the Roe's upwind scheme [16] is used. The numerical flux of the inviscid terms across each cell face $\boldsymbol{k}$ using Roe's flux-difference splitting can be written as

$$\boldsymbol{F}_k=\tfrac{1}{2}[\boldsymbol{F}(\boldsymbol{Q}_L)+\boldsymbol{F}(\boldsymbol{Q}_R)-\left|\tilde{\boldsymbol{A}}\right|(\boldsymbol{Q}_R-\boldsymbol{Q}_L)]_k \qquad (2)$$

where $\tilde{A}$ is the Roe-averaged flux Jacobian matrix ($A=\partial\boldsymbol{F}/\partial\boldsymbol{Q}$) and $\boldsymbol{Q}_L$ and $\boldsymbol{Q}_R$ are the state variables to the left and right of the interface $\boldsymbol{k}$, and

$$\left|\tilde{\boldsymbol{A}}\right|(\boldsymbol{Q}_R-\boldsymbol{Q}_L)=\left|\Delta\tilde{\boldsymbol{F}}_1\right|+\left|\Delta\tilde{\boldsymbol{F}}_2\right|+\left|\Delta\tilde{\boldsymbol{F}}_3\right|$$

$$\left|\Delta\tilde{\boldsymbol{F}}_1\right| = \left|\tilde{U}_{\perp r}\right|\left\{(\Delta\rho - \frac{\Delta p}{\tilde{a}^2})\begin{bmatrix}1\\ \tilde{u}\\ \tilde{v}\\ \tilde{w}\\ \frac{(\tilde{u}^2+\tilde{v}^2+\tilde{w}^2)}{2}\end{bmatrix} + \tilde{\rho}\begin{bmatrix}0\\ \Delta u - \hat{n}_x\,\Delta U_{\perp r}\\ \Delta v - \hat{n}_y\,\Delta U_{\perp r}\\ \Delta w - \hat{n}_z\,\Delta U_{\perp r}\\ \tilde{u}\Delta u + \tilde{v}\Delta v + \tilde{w}\Delta w - \tilde{U}_\perp\,\Delta U_{\perp r}\end{bmatrix}\right\}$$

$$\left|\Delta\tilde{\boldsymbol{F}}_{2,3}\right| = \left|\tilde{U}_{\perp r} \pm \tilde{a}\right|\left(\frac{\Delta p \pm \tilde{\rho}\,\tilde{a}\,\Delta U_{\perp r}}{2\,\tilde{a}^2}\right)\begin{bmatrix}1\\ \tilde{u} \pm \hat{n}_x\,\tilde{a}\\ \tilde{v} \pm \hat{n}_y\,\tilde{a}\\ \tilde{w} \pm \hat{n}_z\,\tilde{a}\\ \tilde{H} \pm \tilde{V}_n\,\tilde{a}\end{bmatrix}$$

where $\Delta(\,) = (\,)_R - (\,)_L$, the superscript $\sim$ denotes Roe-averaged quantities, $H = (E + p)/\rho$ is the total enthalpy, a is the speed of sound and

$$\Delta U_{\perp r} = \hat{n}_x\Delta u + \hat{n}_y\Delta v + \hat{n}_z\Delta w$$
$$\tilde{U}_\perp = \tilde{u}\hat{n}_x + \tilde{v}\hat{n}_y + \tilde{w}\hat{n}_z$$

The left and right states $\boldsymbol{Q}_L$ and $\boldsymbol{Q}_R$ are computed by upwind-biased interpolation of the primitive variables $\boldsymbol{q} = [\rho, u, v, w, p]^T$. For a first-order scheme, the state of the primitive variables $\boldsymbol{q}$ at each cell face is set to the cell-centered average on either side of the face. High-order accuracy is achieved via the reconstruction of flow variables using the MUSCL interpolation technique [17]

$$\begin{aligned}\boldsymbol{q}_L &= \boldsymbol{q}_j + \frac{s}{4}[(1-\kappa s)\nabla_j + (1+\kappa s)\Delta_j]\\ \boldsymbol{q}_R &= \boldsymbol{q}_{j+1} - \frac{s}{4}[(1+\kappa s)\nabla_{j+1} + (1-\kappa s)\Delta_{j+1}]\end{aligned} \tag{3}$$

where $\kappa = -1$ is used for the second-order accuracy. The symbols ∇ and Δ are backward and forward difference operators, respectively, and s is the flux limiter to ensure the monotone interpolation. For computing rotor flows in transonic regime, oscillations in the numerical solution near shock wave are expected to occur. To eliminate these oscillations and prevent nonphysical solution, a continuously differentiable flux limiter is employed [22]

$$s = \frac{2\nabla\Delta + \varepsilon}{\nabla^2 + \Delta^2 + \varepsilon} \tag{4}$$

where ε is a very small constant, typically $\varepsilon = 1.0^{-6}$, used to prevent the division by zero in smooth regions of the flow.

4 Time Integration

A semidiscrete form of the governing equations for each cell can be written as

$$V_j\frac{\Delta\boldsymbol{Q}_j}{\Delta t} = \boldsymbol{R}_j, \qquad j = 1, 2, 3, \ldots \tag{5}$$

where

$$\boldsymbol{R}_j = \left\{\boldsymbol{S}(\boldsymbol{Q})V\right\}_j - \sum_{i=k\ (j)}\boldsymbol{F}_{j,i}\,\Delta S_{j,i},$$

and V_j is the cell volume and $\boldsymbol{R}_j$ is the residual accrued by summation of the inviscid fluxes through the four faces k of a tetrahedral cell j. The explicit scheme is obtained by evaluating the total residual at the right-hand side of Eq. (5) at the time level n. For time integration, the classical fourth-order Runge-Kutta scheme [23] may be implemented to achieve time accuracy and stabilize governing equations. For the present calculations, only steady state solutions are considered and time accuracy in the integration is not required. Here, the first-order Euler explicit scheme is used and the solution convergence to steady state is accelerated by implicit residual smoothing.

5 Boundary Conditions

At every time step, one should specify the boundary conditions at the blade surface and the far field boundaries. At the blade surface, the flow tangency condition is used for inviscid flows. The slip boundary condition is implemented by imposing no flux through the

wall by setting the flow variables within dummy cells that are effectively inside the blade surface. The relative velocity components within a dummy cell, $(u_r, v_r, w_r)_d$, are evaluated from the values in the cell j adjacent to the surface, $(u_r, v_r, w_r)_j$, as follows [22]

$$\begin{Bmatrix} u_r \\ v_r \\ w_r \end{Bmatrix}_d = \begin{bmatrix} 1-2\hat{n}_x^2 & -2\hat{n}_x\hat{n}_y & -2\hat{n}_x\hat{n}_z \\ -2\hat{n}_x\hat{n}_y & 1-2\hat{n}_y^2 & -2\hat{n}_y\hat{n}_z \\ -2\hat{n}_x\hat{n}_z & -2\hat{n}_y\hat{n}_z & 1-2\hat{n}_z^2 \end{bmatrix} \begin{Bmatrix} u_r \\ v_r \\ w_r \end{Bmatrix}_j$$

where $\hat{\boldsymbol{n}}(\hat{n}_x, \hat{n}_y, \hat{n}_z)$ is the unit vector normal to the boundary face. Also, the density and the pressure within the dummy cell are set equal to the values in the cell adjacent to the surface.

The far field boundary conditions are applied at a finite distance from the blade surface. The treatment of the far-field boundary condition is based on the one-dimensional Reimann invariants normal to the far field boundary. This procedure correctly accounts for wave propagation in the far field which is important for fast convergence to steady state solution. For the far field boundary where the flow is subsonic, the fixed and extrapolated Riemann invariants corresponding to incoming and outgoing waves are introduced

$$R_\infty = V_{n\infty} - \frac{2a_\infty}{\gamma - 1}, \qquad R_e = V_{ne} + \frac{2a_e}{\gamma - 1} \tag{6}$$

Then, the actual normal velocity V_n and the speed of sound a in the far field are obtained by adding and subtracting the preceding invariants as follows

$$V_n = \frac{1}{2}(R_e + R_\infty), \qquad a = \frac{1}{4}(\gamma - 1)(R_e - R_\infty)$$

As an outflow boundary, the tangential velocity component and entropy are extrapolated from the interior, while at an inflow boundary, they are specified using far field values.

6 Prescribed Wake Model

For full free wake modeling, whole rotor wake including the inboard vortex sheet and the tip vortex trailing from each blade, must be tracked for many rotor revolutions to properly predict

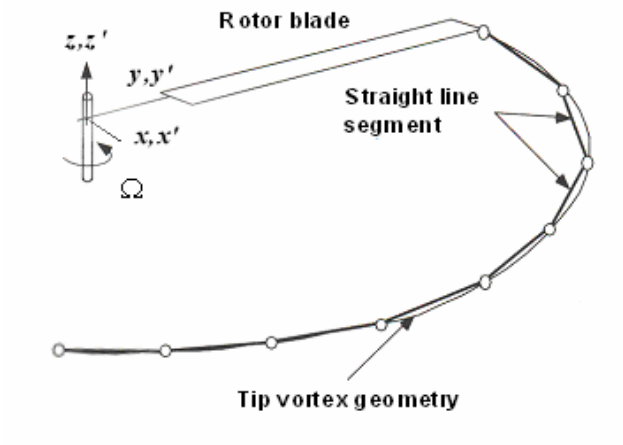

Fig. 1 Geometry of the tip vortex trailed from tip of each blade.

the effects of rotor wake. Although full free wake modeling will give an accurate solution of the rotor wake, this is computationally difficult to do and very time consuming. For computational economy, however, it is usually only necessary to model the blade tip vortices that will result in a minor loss of accuracy of the rotor wake effects.

In the present study, the wake effects of each blade are modeled using only a tip vortex trailed at the tip of each blade (Fig. 1) and the effects of inboard vortex sheet is modeled implicitly by reducing the strength of the tip vortex. The initial geometry of tip vortex is constructed using the prescribed wake model introduced by Landgreb [19,20]. For this wake model, the axial and radial coordinates of the tip vortex are, respectively,

$$\frac{z_{tip}}{R} = \begin{cases} k_1\psi_w & 0 \le \psi_w \le \dfrac{2\pi}{N_b} \\ \left.\dfrac{z_{tip}}{R}\right|_{\psi_w = \frac{2\pi}{N_b}} + k_2(\psi_w - \dfrac{2\pi}{N_b}) & \psi_w \ge \dfrac{2\pi}{N_b} \end{cases} \tag{7}$$

$$\frac{y_{tip}}{R} = r_{tip} = A + (1 - A)\exp(-\Upsilon\,\psi_w)$$

and

$$k_1 = -0.25\,(C_T / \sigma + 0.001\,\theta_{tw})$$

$$k_2 = -(1.41 + 0.0141\,\theta_{tw})\sqrt{C_T / 2}$$

where ψ_w is the age angle, N_b is the number of blades, R is the rotor radius, θ_{tw} is the value of blade twist, σ is the rotor solidity and C_T is the thrust coefficient. Also, A is the contraction ratio of the wake, its experimental value is 0.78 and Υ can be obtained by

$$\Upsilon = 0.145 + 27\,C_T$$

To calculate the induced velocity caused by the wake effects and incorporate these effects into the Euler solver, the geometry of the vortex trailed from the tip of each blade is discretized to vortex filaments that are linked together using a piecewise linear reconstruction (Fig. 1). Assuming the flow is predominately incompressible, according to Helmholtz third law, the net circulation strength of the each tip vortex is constant across the filaments. The induced velocity associated with each vortex filament can be computed by the Biot-Savart law

$$\boldsymbol{V}_0 = \frac{\Gamma}{4\pi}\frac{d\boldsymbol{l}\times\boldsymbol{r}}{|r|^3} \qquad (8)$$

where $d\boldsymbol{l}$ is the differential element of prescribed wake geometry, Γ is the circulation and $\boldsymbol{r}$ is the vector connecting between the wake filament and centeriod of the cell. In the present computations, to account for the effects of inboard vortex sheet, the strength of tip vortex is determined by %80 of the maximum bound circulation on the blade span.

7 Perturbation Method

As mentioned before, the artificial viscosity required for numerical stability, especially for course grids (Fig. 2), causes the rotor wake to be smeared as the vortices are convected away the rotor disk. Therefore, a sufficiently fine grid is needed to reduce the level of numerical diffusion of vorticity and resolve the structure of the rotor wake. This usually leads to large computational time and high memory required.

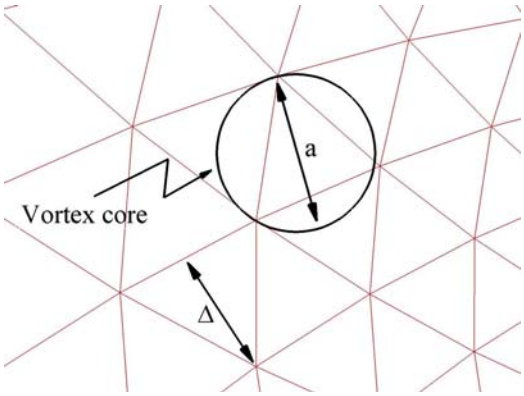

Fig. 2 Comparison of vortex core size with far field grid resolution for an unstructured grid.

An alternative way is to use a perturbation scheme [14,18]. In this method, the structure of rotor wake and its location may be specified without the need to utilize a sufficiently fine grid to resolve the rapid flow gradients. The idea of the perturbation method is that for some region, the flowfield is dominated locally by the velocity field associated with the rotor wake and the effect of rotor blade is weak near the wake region.

In the present study, the rotor wake is modeled only by the tip vortices. Using the induced velocity field of the tip vortices, a state vector $\boldsymbol{Q_0} = [\rho_0, \rho_0 u_0, \rho_0 v_0, \rho_0 w_0, E_0]^T$ that approximately satisfies the steady Euler equations can be readily calculated. Then, by subtracting the flux integral associated with this state vector from Eq. (1), the resulting integral equation can be written as follows

$$\frac{\partial}{\partial t}\iiint_V \boldsymbol{Q}\,dV + \iint_{\partial V}\{\boldsymbol{F}(\boldsymbol{Q}) - \boldsymbol{F}(\boldsymbol{Q_0})\}.\hat{n}\,dS = \iiint_V \{\boldsymbol{S}(\boldsymbol{Q}) - \boldsymbol{S}(\boldsymbol{Q_0})\}\,dV \qquad (9)$$

The surface integral associated with the flowfield $\boldsymbol{Q_0}$ is zero. However, $\boldsymbol{Q_0}$ will not necessarily satisfy the discrete equations due to the truncation error, and for a fine grid, this term will be small.

By applying the discrete spatial operator, Eq. (5), to the flowfield $\boldsymbol{Q_0}$, the residual $\boldsymbol{R_0}$ is calculated at each cell. Therefore, by subtracting

the residual $\boldsymbol{R_0}$ from the residual $\boldsymbol{R}$ due to the complete state vector $\boldsymbol{Q}$, the following discrete Euler equations are obtained

$$V_j \frac{\Delta \boldsymbol{Q}_j}{\Delta t} = (\boldsymbol{R} - \boldsymbol{R}_0)_j = \left\{\left[\boldsymbol{S}(\boldsymbol{Q}) - \boldsymbol{S}(\boldsymbol{Q_0})\right]V\right\}_j - \sum_{i=k\ (j)} \left(\boldsymbol{F}_{j,i} - \boldsymbol{F}_{0_{j,i}}\right)\Delta S_{j,i}, \quad j = 1, 2, 3, \ldots \tag{10}$$

It is clear that the residual $\boldsymbol{R}$ is driven to $\boldsymbol{R_0}$ at the steady state condition. Therefore, the truncation error of the scheme can be corrected in the region of the tip vortices, and the state vector $\boldsymbol{Q}$ and the associated residual $\boldsymbol{R}$ should show similar behavior as $\boldsymbol{Q_0}$ and $\boldsymbol{R_0}$. Away from the region of tip vortices, the residual $\boldsymbol{R_0}$ will be small, because the gradients of the flowfield are weak and hence, the solution in these regions will be the same as the solution associated with the regular finite-volume method.

8 Results and Discussion

The developed Euler code has been thoroughly verified by comparison with available numerical solutions and experimental results for the case of nonrotating body. These verifications include transonic flow at a freestream Mach number of $M_\infty = 0.84$ and an angle of attack of $\alpha = 8°$ over ONERA M6 wing and supersonic flow over a secant ogive cylinder bottailed (SOCBT) body at $M_\infty = 3.0$. The results of the developed Euler code are in good agreement with the available results. Details of these investigations have been reported in Ref. 24.

To show the efficiency and accuracy of the present flow solver, the inviscid flowfield is computed for an isolated rotor in hover. This test case was experimentally studied by Caradona and Tung [21]. The experimental model consists of a two-bladed rigid rotor with rectangular planform blades with no twist or taper. The blades are made of NACA 0012 airfoil sections with an aspect ratio of 6. Calculations are performed for the two operating conditions of subsonic and transonic

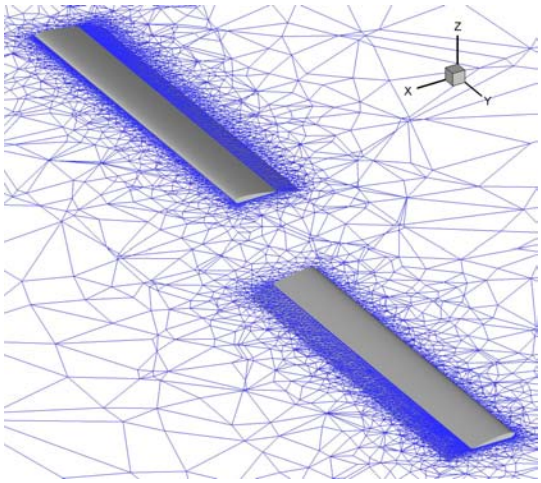

(b)

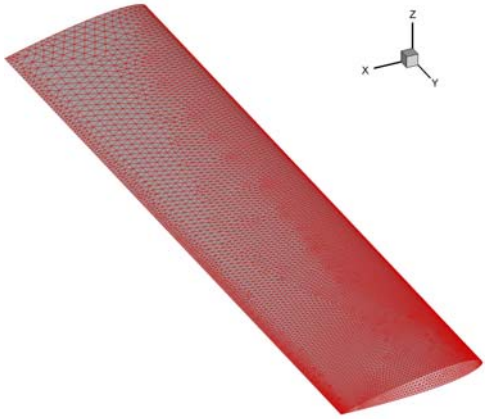

(a)

Fig. 3 (a) Blade surface triangulation and (b) computational grids for Caradonna and Tung test case.

tip Mach numbers, $M_{tip} = 0.44$ and $M_{tip} = 0.877$, and for the collective pitch angle $\alpha = 8°$. Surface pressure data are available at a number of chordwise locations and at several radial stations for code validation. The results using the present flow solver are compared with numerical and experimental results and the effects of wake modeling on the flowfield characteristics are investigated

Figure 3 shows the blade surface triangulation and also computational grid for the Caradonna and Tung test cases. The computational domain consists of unstructured tetrahedral cells using a Delaunay method. The

grid is chosen to be fine at the leading and trailing edges especially at the tip region of the blades (Fig. 3a). The three-dimensional grid consists of 474551 tetrahedral and 97457 node points. The surface triangulation on the blade surface consists of 69762 triangles. The far field boundary is a sphere with 30 radii away from the center of rotation. For unstructured grids, without an adaptation procedure, usually course grids are generated far away from the body surface (Fig 3b). For rotor flows using conventional grids and without using a wake modeling, the vortical wake effects can not be accurately simulated. This can be found by comparing the results of the blade surface pressures using the wake modeling and without any wake modeling.

Figure 4 compares the computed surface pressure coefficient using the second-order solution with the experimental data at different spanwise locations. The calculations are presented for both subsonic and transonic tip Mach numbers. The results indicate that without wake modeling, the computed pressure distributions for the inboard sections of the blade are not in agreement with those of experiment. This may be due to the numerical viscosity present in the conventional numerical schemes, particularly on course grids. As a result, due to improper capturing of the vortical wake, the induced flowfield can not be accurately computed. It causes to increase the angle of attack of the blades in inboard sections where the computed pressure distributions do not match with the experimental results.

Figure 5 demonstrates the effect of wake modeling using the proposed method on the computed surface pressure coefficient at different stations for the subsonic case, $M_{tip} = 0.44$. The geometry of prescribed tip vortex is constructed using the prescribed wake model introduced by Landgreb. The resulting pressure distributions using the proposed prescribed wake-Euler solver exhibit good agreement with the experimental data at all sections. It is seen that the free wake model improves the quality of the solution. The results are also compared with those of Agarwal and

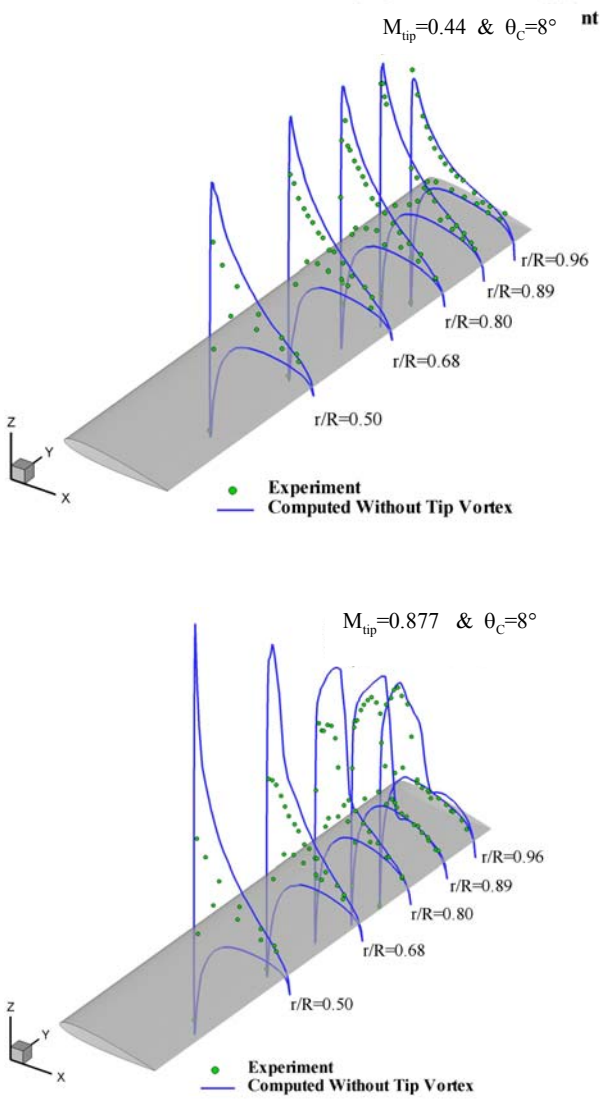

Fig. 4 Comparison of surface pressure coefficient for 2nd order solution and experimental data at different stations for two tip Mach numbers.

Deese [25]. They solved the Euler equations for the flowfield around the rotor using a Jameson's scheme. They used the results of a free wake solution to calculate the induced angle of attack for each section of the rotor blade and then correct the geometric angle of attack of the blade at all stations to account for the wake influence. It is found that the present results without the wake modeling exhibit good agreement with those of Agarwal and Deese. This may be due to good performance of the present solution or high level of artificial

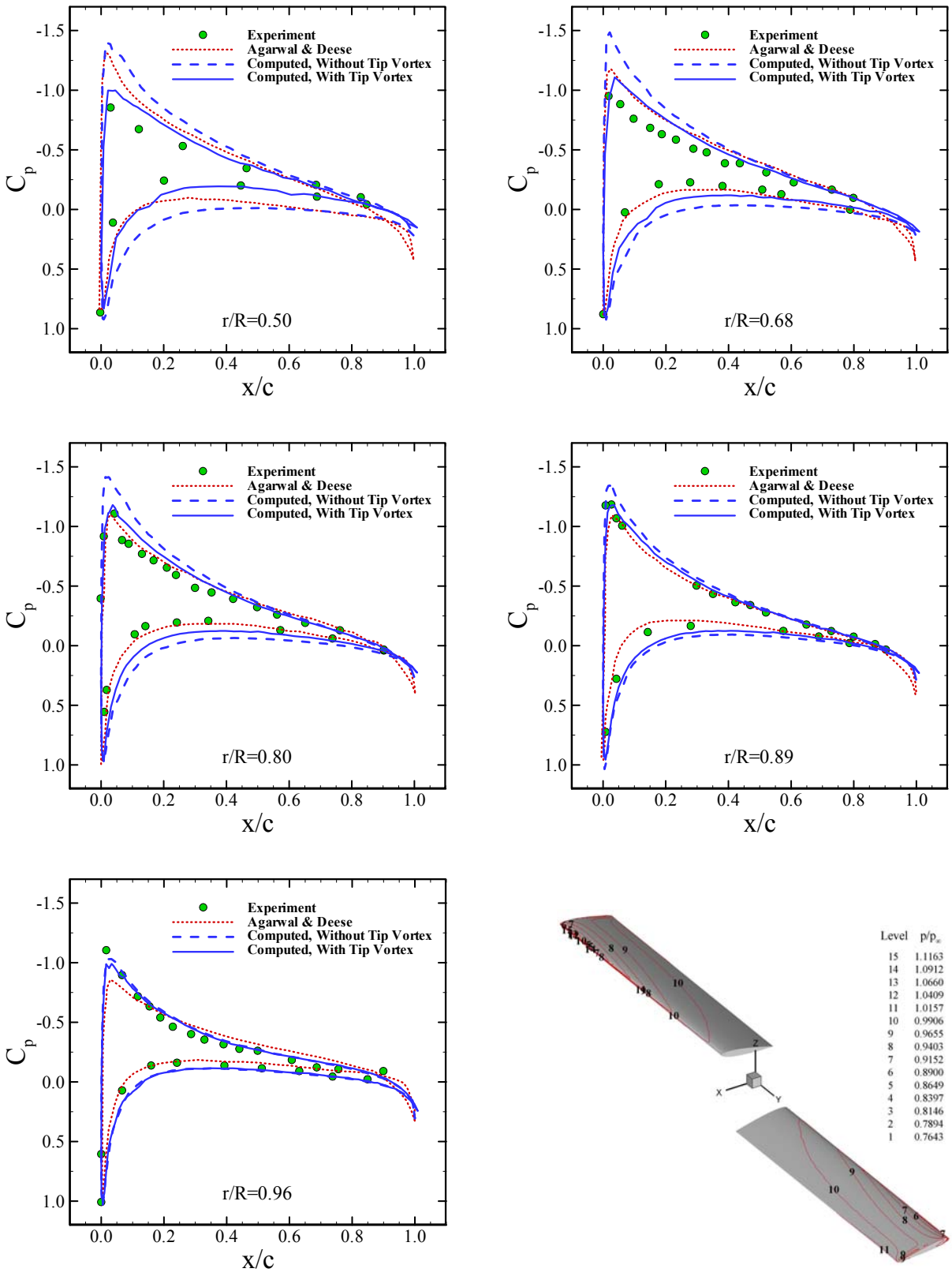

Fig. 5 Effect of wake modeling on computed surface pressure coefficient for $M_{tip} = 0.44$ and collective pitch angle $\theta_c = 8^\circ$

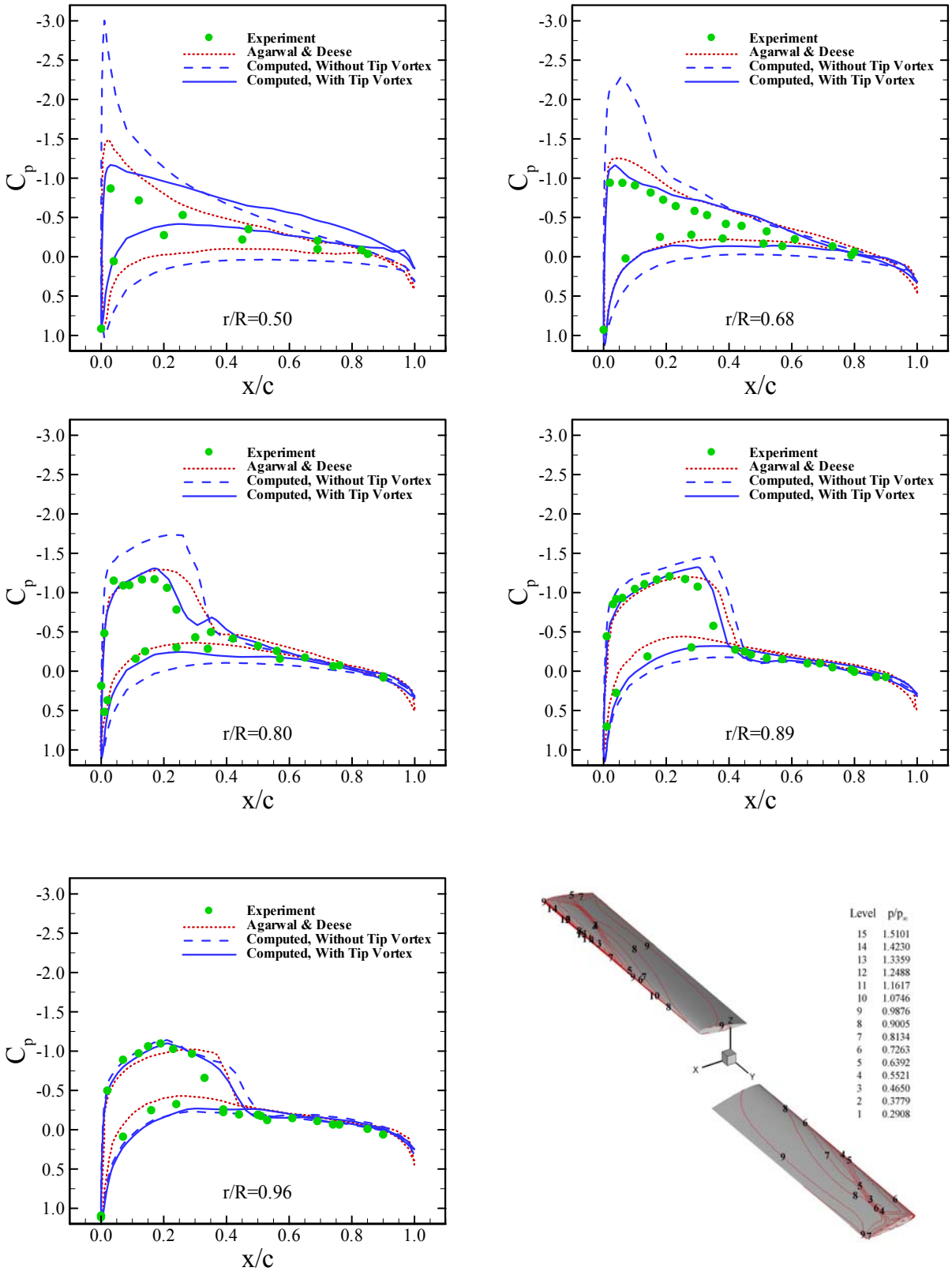

Fig. 6 Effect of wake modeling on computed surface pressure coefficient for $M_{tip} = 0.877$ and collective pitch angle $\theta_c = 8^\circ$

diffusion present in their numerical method. It is also clear that the present wake modeling improves the results considerably. The present prescribed wake-Euler solver uses only the tip vortices for the wake modeling instead of a full free wake modeling, and therefore can be efficiently applied to account for the vortical wake effects of rotor flow in hover. Figure 5 also shows the surface pressure contours for the case of subsonic tip speed. From the figure the effect of radially increasing speed can be observed.

The proposed method is also applied to the transonic case, $M_{tip} = 0.877$, to examine the accuracy and validity of the results. Figure 6 shows the computed surface pressure coefficient at five radial stations. The agreement of the pressure distributions computed by using the proposed technique with the experimental data and the results of Agarwal and Deese is good, especially for the outboard region ($r/R > 0.5$). The difference for the inboard stations may be due to the effect of inboard vortex sheet which is not considered in the present solution. It is also obvious that the transonic regions near the tip of the blades are accurately computed. In Fig. 6, the surface pressure contours for this case is also shown. The effects of radially increasing speed and transonic regions at the outboard stations of the blades and the corresponding shock wave are evident.

9 Concluding Remarks

A coupled prescribed wake-Euler solver has been developed to compute inviscid flow around rotor under hovering conditions. The aerodynamic characteristics including the surface pressure distributions for both subsonic and transonic conditions are compared with available numerical and experimental data. The results indicate for conventional grids and without wake modeling, the calculated pressure distributions especially at inboard sections of the blades are not in agreement with experimental data. This may be due the presence of the numerical dissipation especially for course grids which can affect the structure of the rotor wake. To improve the predicted results, a perturbation method has been used and wake effects are modeled using only a tip vortex trailed from the tip of each blade. The resulting surface pressure distributions exhibit excellent agreement with the numerical and experimental results especially for subsonic conditions. For the transonic condition small deviations exist for the inboard region, however, the transonic regions and corresponding shock wave are accurately computed. The present methodology introduces a useful and efficient solver for simulating hovering helicopter rotor flow instead of a more complete wake modeling, especially for subsonic conditions.

References

[1] Richason, T. F. and Katz, J., "Unsteady Panel Method for Flows with Multiple Bodies Moving Along Various Paths," *AIAA Journal*. Vol. 32, No. 1, pp. 62-68, 1994.

[2] Ahmed, S. R. and Vidjaja, V. T., "Unsteady Panel Method Calculation of Pressure Distribution on BO 105 Model Rotor Blades," *Journal of the American Helicopter Society*, 1998.

[3] Tang, L., and Baeder, J. D., "Improved Euler Simulation of Hovering Rotor Tip Vortices with Validation," *AHS 55th Annual Forum*, Montreal, Canada, 1999.

[4] Hall, C. M., Long, L. N., "High-Order Accurate Simulations of Wake and Tip Vortex Flowfields," *AHS 55th Annual Forum*, Montreal, Canada, 1999.

[5] Hariharan, N. and Sankar, L. N., "First-Principles Based High Order Methodologies for Rotorcraft Flowfield Studies," *AHS 55th Annual Forum*, Montreal, Canada, 1999.

[6] Hariharan, N., Sankar, L. N., "Higher Order Numerical Simulation of Rotor Flow Field," *AHS Forum and Technology Display*, Washington, DC., 1994.

[7] Hariharan, N., "Evaluation of High Order Upwind Schemes for Rotors in Hover," AIAA Paper 2003-49, 2003.

[8] Kang H. J. and Kwon O. J., "Effect of Wake Adaptation on Rotor Hover Simulations Using Unstructured Meshes," *Journal of Aircraft*. Vol. 38, No. 5, pp. 868-877, 2001.

[9] Kang H. J. and Kwon O. J., "Unstructured Mesh Navier-Stokes Calculation of the Flow Field of a Helicopter Rotor in Hover," *Journal of the American Helicopter Society*. April, pp. 90-99, 2002.

[10] Berkman, M. E., Sankar, L. N., Berezin, C. R., and Torok, M. S., "A Navier-Stokes/Full Potential/Free Wake Method for Advancing Multi-Blade Rotors." *Proceedings of the 53th Annual Forum of the American Helicopter Society*. Virginia Beach, VA., 1997.

[11] Moulton, M. A., Wenren, Y., Caradonna, F. X., "Free-Wake Hover Flow Prediction with a Hybrid Potential/Navier-Stokes Solver." *AHS 55th Annual Forum*, Montreal, Canada, 1999.

[12] Hariharan, N., Sankar, L. N., "A Review of Computational Techniques for Rotor Wake Modeling." AIAA Paper 2000-0114, 2000.

[13] Strawn, R. C., and M. J. Djomehri, "Computaional Modeling of Hovering Rotor and Wake Aerodynamics," *Journal of Aircraft*, Vol. 39, No. 5, Sept.-Oct. 2002.

[14] Roberts, T. W., "Euler Equation Computations for the Flow over a Hovering Helicopter Rotor," Ph.D. Dissertation, Department of Aeronautics and Astronautics, The Massachusetts Institute of Technology, Nov. 1986.

[15] Cao, Y., Yu, Z., and Su, Y., "A Coupled Free Wake-CFD Method for the Simulation of Helicopter Rotor Flow," *Canadian Aeronautics and Space Journal*, Vol. 48, No. 4, Dec. 2002.

[16] Roe, P. L., "Characteristic-Based Schemes for the Euler Equations," *Annual Review of Fluid Mechanics*, Vol. 18, pp. 337-365, 1986.

[17] Van Leer, B., "Towards the Ultimate Conservative Difference Scheme, V: A Second Order Sequel to Godunov's Method," *Journal of Computational Physics*, Vol. 32, 1979, pp. 101-136.

[18] Chow, L. J. and Pulliam, T. H. and Steger, J. L., "A General Perturbation Approach for the Equation of Fluid Dynamics," AIAA Paper 83-1903CP, 1983.

[19] Landgrebe, A. J., "An Analytical and Experimental Investigation of Helicopter Rotor Performance and Wake Geometry Characteristic," USAAMRDL TR 71-24, 1971.

[20] Landgrebe, A.J. (1972). "The Wake Geometry of a Hovering Helicopter Rotor and Its Influence on Rotor Performance". *J. Am. Helicopter Soc*. Vol. 17, No. 4. pp. 3–15.

[21] Caradonna, F. X. and Tung. C., "Experimental and Analytical Studies of a Model Helicopter Rotor in Hover," *Vertica*, Vol. 5, pp. 149-161, 1981.

[22] Batina, J. T., "Implicit Upwind Solution Algorithms for Three-Dimensional Unstructured Meshes," *AIAA Journal,* Vol. 31, No. 5, pp. 801-805, 1993.

[23] Jameson, A. and Schemidt, W. and Turkel, E., "Numerical Solution of the Euler Equations by Finite Volume Methods using Runge-Kutta Time Stepping Schemes," AIAA Paper 81-1259, 1981.

[24] Hejranfar, K. and Mohammadi, M., "Upwind Scheme for Solution of Three-Dimensional Inviscid Flows over Complex Geometries on Unstructured Meshes," *Proceedings of the 9th Fluid Dynamics Conference*, Iran, Shiraz, March 2005.

[25] Agarwal, R. K. and Deese, J. E., "Euler Calculations for Flowfield of a Helicopter Rotor in Hover," *Journal of Aircraft*, Vol. 24, No.4, pp. 231-238, 1987.